JACS Au
AN OPEN ACCESS JOURNAL OF THE AMERICAN CHEMICAL SOCIETY

pubs.acs.org/jacsau
Article

Optimizing the Lattice Nitrogen Coordination to Break the Performance Limitation of Metal Nitrides for Electrocatalytic Nitrogen Reduction

Haiyang Yuan, Chen Zhu, Yu Hou, Hua Gui Yang, and Haifeng Wang*

Cite This: JACS Au 2024, 4, 3038−3048

Read Online

ACCESS | Metrics & More | Article Recommendations | Supporting Information

ABSTRACT: Metal nitrides (MNs) are attracting enormous attention in the electrocatalytic nitrogen reduction reaction (NRR) because of their rich lattice nitrogen (N_{lat}) and the unique ability of N_{lat} vacancies to activate N_2. However, continuing controversy exists on whether MNs are catalytically active for NRR or produce NH_3 via the reductive decomposition of N_{lat} without N_2 activation in the in situ electrochemical conditions, let alone the rational design of high-performance MN catalysts. Herein, we focus on the common rocksalt-type MN(100) catalysts and establish a quantitative theoretical framework based on the first-principles microkinetic simulations to resolve these puzzles. The results show that the Mars-van Krevelen mechanism is kinetically more favorable to drive the NRR on a majority of MNs, in which N_{lat} plays a pivotal role in achieving the Volmer process and N_2 activation. In terms of stability, activity, and selectivity, we find that MN(100) with moderate formation energy of N_{lat} vacancy (E_{vac}) can achieve maximum activity and maintain electrochemical stability, while low- or high-E_{vac} ones are either unstable or catalytically less active. Unfortunately, owing to the five-coordinate structural feature of N_{lat} on rocksalt-type MN(100), this maximum activity is limited to a yield of NH_3 of only $\sim 10^{-15}$ mol s^{-1} cm^{-2}. Intriguingly, we identify a volcano-type activity-regulating role of the local structural features of N_{lat} and show that the four-coordinate N_{lat} can exhibit optimal activity and overcome the performance limitation, while less coordinated N_{lat} fails. This work provides, arguably for the first time, an in-depth theoretical insight into the activity and stability paradox of MNs for NRR and underlines the importance of reaction kinetic assessment in comparison with the prevailing simple thermodynamic analysis.

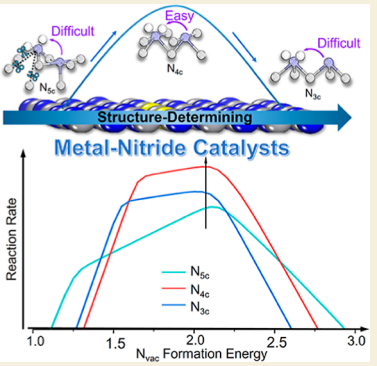

KEYWORDS: *electrocatalytic nitrogen reduction, metal nitrides, activity limitation, surface topology, density functional theory calculation, microkinetic*

INTRODUCTION

The ammonia synthesis is one of the most critical reactions in modern industry.[1−5] The Haber-Bosch process as the primary route to produce NH_3 is energy-intensive.[6,7] The electrosynthesis offers a promising strategy to produce NH_3 at mild conditions, such as lithium-mediated ammonia synthesis, nitrate/NO_x reduction and direct N_2 reduction reaction [nitrogen reduction reaction (NRR)],[8−12] in which the direct NRR is the most attractive technology.[13] Unfortunately, although much effort has been made to develop superior catalysts for NRR,[13−30] many of them are demonstrated to produce only tiny amounts of NH_3 or even do not produce NH_3 under the protocols with rigorous isotope labeling experiments.[9,31−33] Therefore, there is a strong desire to design and prepare advanced catalysts for NRR or at least provide a relatively explicit direction for optimizing catalysts.

Metal nitrides (MNs), which can provide rich lattice nitrogens (N_{lat}) to form NH_3 and abundant N_{lat} vacancies to activate N_2, have been widely tested in experiments for nitrogen reduction.[17−26,34,35] In electrocatalytic NRR, one of the most significant ambiguities for MNs is where NH_3 comes from, i.e., the decomposition of N_{lat} or the catalytic reduction of N_2.[36−39] Whether MNs are suitable for electrocatalytic NRR has been confused. For example, VN, which possesses good conductivity and has been used for oxygen electroreduction,[40,41] was synthesized by some research groups and demonstrated to be efficient in the electrosynthesis of NH_3 with high selectivity (vs H_2 evolution reaction, HER).[22,23] However, under the rigorous testing protocols, some studies found that the inability of VN to catalyze the electrosynthesis of NH_3 from N_2 and VN could release N_{lat} in a noncatalytic process, leading to the formation of NH_3.[36−38] A similar controversy exists for Mo_2N catalyst.[26,39] These different observations could be due to different fine structures exposed under different preparation conditions;[36] for example, all facets of VN except (100) were predicted to show a faster migration

Received: April 27, 2024
Revised: August 8, 2024
Accepted: August 12, 2024
Published: August 15, 2024

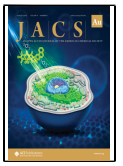

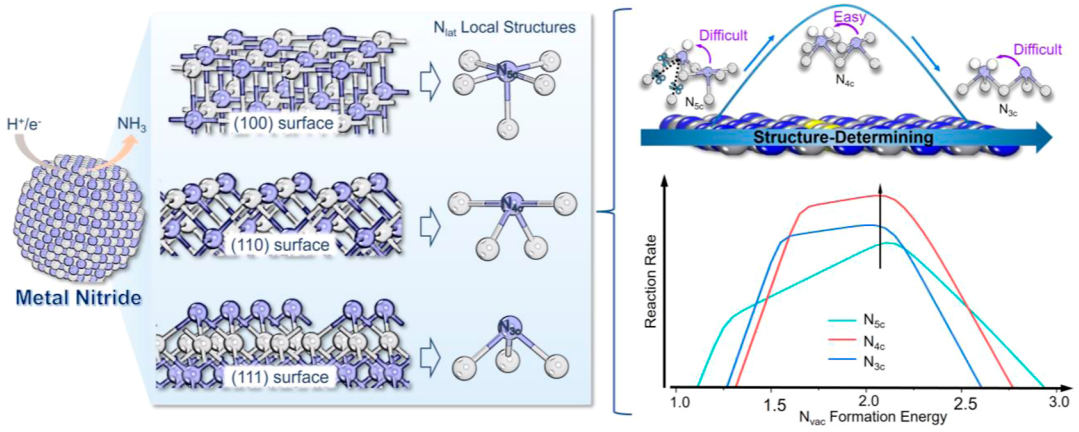

Figure 1. Major scientific problem and the key findings of this work. The fine structure of the lattice N_{lat} is an important factor determining the activity and ability of MNs for NRR. The four-coordinate N_{lat} (N_{4c}) can exhibit optimal activity and overcome the performance limitation.

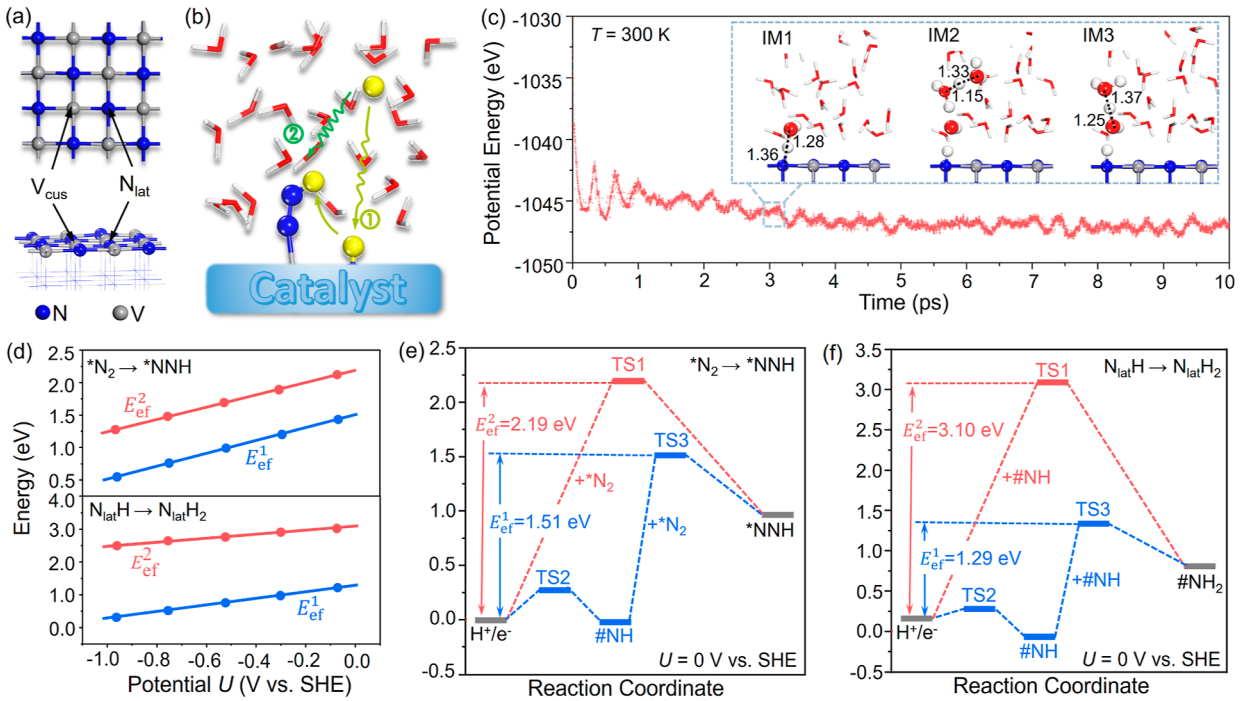

Figure 2. (a) Structure of rocksalt-VN(100) surface. (b) Routes of aqueous H^+ attack the reactant. Route i, the proton transfers to the catalyst surface via the Volmer process ($H^+ + e^- \rightarrow H_{ads}$) first, and then the adsorbed H_{ads} species reacts with the adsorbed reactant (H_{ads} + *R → *RH, where R represents reactant); Route ii, the proton directly attacks reactant adsorbed on the catalyst surface by the proton-coupled electron transfer process (PCET, $H^+ + e^- + R \rightarrow RH$). (c) Potential energy variation from AIMD simulation for water(H_3O^+)/VN(100) system as a function of time. IM1-IM3 are the key states of proton transfer to N_{lat} at 3.100, 3.160, and 3.165 ps, respectively, and the dynamic trajectories can be seen in Figure S2. (d) Relationships of the potential dependent effective barriers of *N_2 → *NNH and $N_{lat}H \rightarrow N_{lat}H_2$ following Route i (E^1_{ef}) and Route ii (E^2_{ef}). (e,f) Energy profiles for *N_2 → *NNH and $N_{lat}H \rightarrow N_{lat}H_2$ following Route i (blue line) and Route ii (red line) at U = 0 V vs SHE, respectively.

than replenishment of N_{lat} vacancies and trend to decompose,[24,38] which may result from the different N_{lat} local structures (Figure 1). One may ask: could the lattice N_{lat} site be essentially active and stable to catalyze the entire cycle of electrocatalytic NRR? Are these conflicting experimental observations structure-dependent? What fine structure could be suitable for electrocatalytic NRR? In terms of these tasks, it is time-consuming and too costly to controllably prepare and measure the NRR performance of each MN individually under the rigorous isotope experimental protocols. Several theoretical studies investigated a series of MN-based materials for NRR and suggested a number of MNs with potential NRR activity by assessing the reaction thermodynamics, such as VN, ZrN, and CrN; these materials potentially exhibit limited HER activity but significantly facilitate N_2 electroreduction due to the presence of N_{lat} vacancies.[24,42−51] However, there appears to be a discrepancy between the theoretical results and the existing experimental results when assessing the catalytic ability of a given MN.[9,31−33,36,37] Therefore, it is crucial to theoretically elucidate the underlying abilities of MNs built on the complete NRR kinetic information and establish the relation between the structural feature and activity/stability based on the kinetic steady-state description. However, the

https://doi.org/10.1021/jacsau.4c00377
JACS Au 2024, 4, 3038−3048

Scheme 1. L−H (a) and MvK (b) Pathways on VN(100), in which the Related Transition State and Intermediate Structures Are Shown in Figures S4−S7[a]

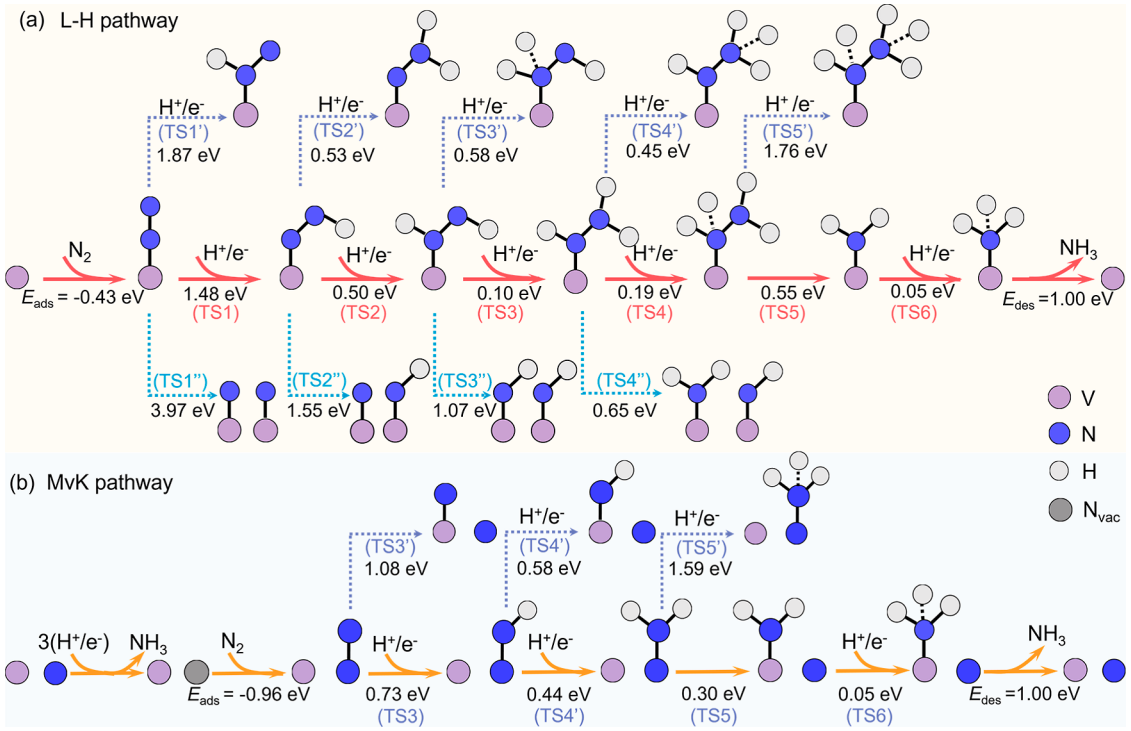

[a]The red and orange lines represent the favored L−H and MvK pathways, respectively (see the detailed energy profiles in Figure S8).

related kinetic analysis was generally ignored in the electrocatalytic NRR simulation.

Toward these challenges, in this work we focused on the most stable (100) surfaces of rocksalt-type MNs (e.g., VN, CrN, TiN, and ZrN) as case catalysts inspired by recent theoretical and experimental studies,[20−24,36,37] aiming to understand the reaction mode of N_{lat} (decomposition or catalysis) in NRR by the first-principles microkinetic analysis. The variation rules of activity and stability of different MNs for NRR were revealed, which shows the optimum activity of rocksalt-type MN(100) at typical working potential at an order of only $\sim 10^{-15}$ mol s^{-1} cm^{-2}, and we further determined the structural origin of this low NRR performance. Importantly, a possible structural feature of N_{lat} on MNs was proposed, i.e., the four-coordinate N_{lat} (denoted as N_{4c}, Figure 1), which may achieve the win−win activity-stability for NRR; the optimal NH_3 yield could be up to $\sim 10^{-11}$ mol s^{-1} cm^{-2}. This work goes beyond the traditional thermodynamic analysis, and the obtained kinetic insight could provide a fundamental direction for MN catalyst optimization.

RESULTS AND DISCUSSION

Electrocatalytic NRR Mechanism on VN Catalyst

To begin with, we took rocksalt-type VN as a case catalyst to gain mechanistic insight into NRR, which is one of the experimentally most attractive and debated MNs.[20−23] The most exposed facet of VN, (100), can be demonstrated by its largest N_{lat} formation energy and lowest surface energy (Table S1), and is terminated by two types of active sites, i.e., the five-coordinate V_{cus} and N_{lat} sites (hereinafter denoted as * and #N, respectively, where # represents the N_{lat} vacancy; Figure 2a). The V_{cus} and N_{lat} sites constitute the basic active sites for NRR, corresponding to two different reaction pathways, respectively: (i) N_2 is activated on the V_{cus} site and completes the Langmuir−Hinshelwood (L−H) pathway; (ii) the N_{lat} is converted into NH_3, followed by N_2 activation in the N_{lat} vacancy, which obeys the so-called Mars-van Krevelen (MvK) pathway involving the removal/refilling of N_{lat}.

Langmuir-Hinshelwood Pathway

As shown in Scheme 1a, N_2 can be activated to some extent at the V_{cus} site with an adsorption energy of −0.43 eV but is difficult to dissociate with a barrier as high as 3.97 eV. Thus, H-mediated N_2 activation is necessary. In this regard, a key issue on the hydrogenating species needs to first be solved, that is how the aqueous proton attacks the reactant (R). Two general routes are illustrated in Figure 2b: (i) the proton transfers to the catalyst surface via the one-electron reduction (Volmer process, $H^+ + e^- \rightarrow H_{ads}$), and then couples with reactant R (H_{ads} + R →RH); (ii) the aqueous proton directly attacks R obeying the proton-coupled electron transfer process (PCET, $H^+ + e^- + R \rightarrow RH$).

It was found that the Volmer process at the V_{cus} or N_{lat} site corresponds to a free energy change of 0.33 and −0.08 eV at U = 0 V (vs the standard hydrogen electrode, SHE), respectively, indicating that the proton prefers to bind to N_{lat} rather than V_{cus}. The ab initio molecular dynamics simulation with the explicit solvation model at T = 300 K shows that H_2O can spontaneously dissociate at the water/VN(100) interface with a H released on N_{lat} and a hydroxyl left on V_{cus}, and then the solvated proton readily transfers to the as-formed hydroxyl through a water molecule chain by the Grotthuss-type mechanism,[52] corresponding to an IM1 → IM2 → IM3 conversion (Figure 2c; see the dynamic trajectories in Figure S2). This indicates that the proton transfer to the VN(100)

https://doi.org/10.1021/jacsau.4c00377
JACS Au 2024, 4, 3038−3048

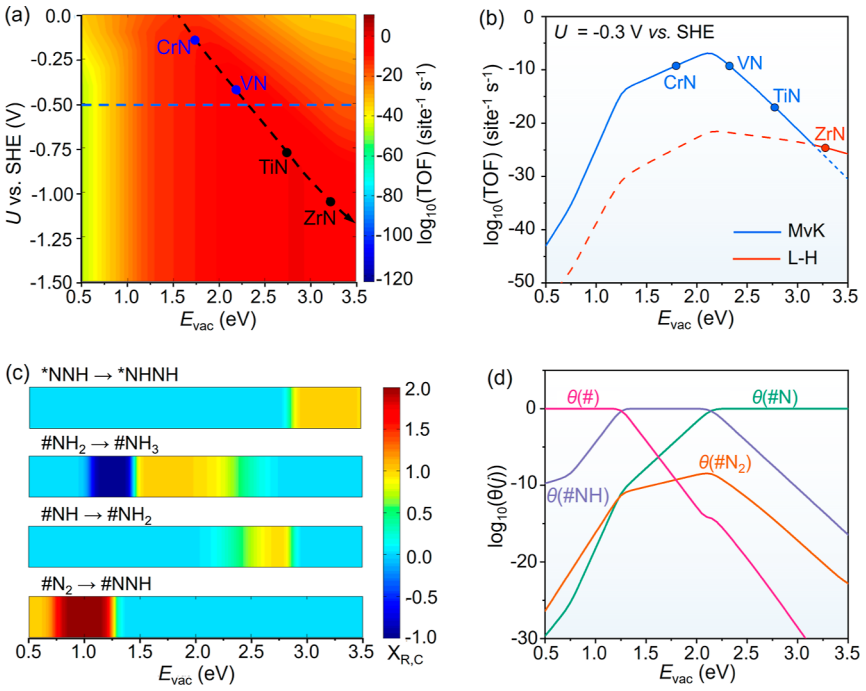

Figure 3. (a) Activity map of NRR following the L−H and MvK pathways as a function of E_{vac} and potential U (vs SHE), where the black dashed line represents the optimal activity trend. (b) Activity curves of NRR at the potential U = −0.3 V, where the red and blue lines represent the L−H and MvK pathways, respectively. (c) Degree of rate control (X_{RC}) change trends of the rate-determining steps in the MvK pathway at the potential U = −0.3 V. (d) Coverage change trends of some important species on MNs at the potential U = −0.3 V.

surface to form $N_{lat}H$ species is a straightforward process. Further, we calculated the reaction barrier of $H^+/e^- + N_{lat} \rightarrow N_{lat}H$ at U = 0 V, and it gives a low energy barrier of only 0.27 eV, implying the kinetic feasibility of this Volmer process.

Below, the reaction kinetics of *NNH formation (*N_2 → *NNH) via Routes i and ii were explored, respectively, where the effect of electrode potential U was included using the charge-extrapolation method (details in Note S1). Figure 2d shows the potential-dependent effective barriers (see details in Note S2), which demonstrate that *N_2 → *NNH via Route i gives an overall lower effective barrier than route ii over a wide range of potentials, indicating the feasibility of Route i. Specifically, as shown in Figure 2e, the effective barrier in Route i is E_{ef}^1 = 1.51 eV at U = 0 V, while the PCET process in Route ii is more difficult with a higher barrier E_{ef}^2 = 2.19 eV. Therefore, it is expected that the $N_{lat}H$ can act as a primary hydrogenating species to complete the subsequent N_2 reduction process.

Based on the above results, we then systematically explored the *N_2 hydrogenation to NH_3 by the L−H pathway (see the detailed discussions in Note S3). As Scheme 1a depicts, the conversion of *N_2 preferentially obeys the associative alternating mechanism, i.e., *N_2 → *NNH → *NHNH → *$NHNH_2$ → *NH_2NH_2. Once *NH_2NH_2 forms, the N−N bond can be split with a low barrier of 0.55 eV, and formed *NH_2 can be easily hydrogenated to release NH_3 and finish the whole catalytic cycle. From Figure S8a, one can see that the first two steps of *N_2 hydrogenating into *NHNH constitute the highest point in the whole energy profile, corresponding to an effective barrier of E_{ef} = 1.74 eV. This implies that the *N_2 hydrogenation could be rate-limiting in the L−H pathway on VN(100).

Mars-van Krevelen Pathway

For comparison, the MvK pathways on the VN(100) catalyst were also systematically examined. For $N_{lat}H$ hydrogenation to $N_{lat}H_2$ ($N_{lat}H \rightarrow N_{lat}H_2$), we first compared the proton attacking routes discussed above. Similarly, Route i, i.e., $N_{lat}H$ resulting from the Volmer process couples with each other, is more favored than Route ii at the typical working potential (Figure 2d,f; see details in Note S2). This further demonstrates that $N_{lat}H$ (#NH) is the main hydrogenating species to participate in NRR. Further hydrogenation of $N_{lat}H_2$ to $N_{lat}H_3$ gives a barrier of 0.44 eV (ΔH = −0.37 eV) and the subsequent release of $N_{lat}H_3$ costs 0.97 eV of energy, leaving an N_{lat} vacancy (N_{vac}).

Remarkably, in comparison with the V_{cus} site, the formed N_{vac} shows a better activation ability toward N_2 with a larger adsorption energy of −0.96 eV (vs −0.46 eV). As Scheme 1b shows (see more details in Note S3), the optimal MvK pathway consists mainly of three key subprocesses: (i) $N_{lat}H$ is hydrogenated to release NH_3 with N_{vac} left, (ii) N_2 adsorbs in the N_{vac} and is hydrogenated to #NNH_2, which then breaks the N−N bond to form *NH_2 and refill the N_{vac} easily (E_a = 0.30 eV), and (iii) *NH_2 is hydrogenated to NH_3, in which the subprocesses i is rate-limiting with an effective barrier of 1.54 eV (Figure S8b). Comparing the L−H and MvK pathways, one can preliminarily judge that the MvK pathway is more feasible with a lower effective barrier on VN(100). A detailed kinetic discussion is given later.

Activity and Stability Analysis of MNs for NRR

To understand the activity and stability trend, we extended the L−H and MvK pathways to other MNs such as CrN, TiN, and ZrN, and calculated the barriers and enthalpy changes of the relevant elementary steps. As the previous studies have shown that the formation energy of oxygen vacancy on metal oxides is

https://doi.org/10.1021/jacsau.4c00377
JACS Au 2024, 4, 3038−3048

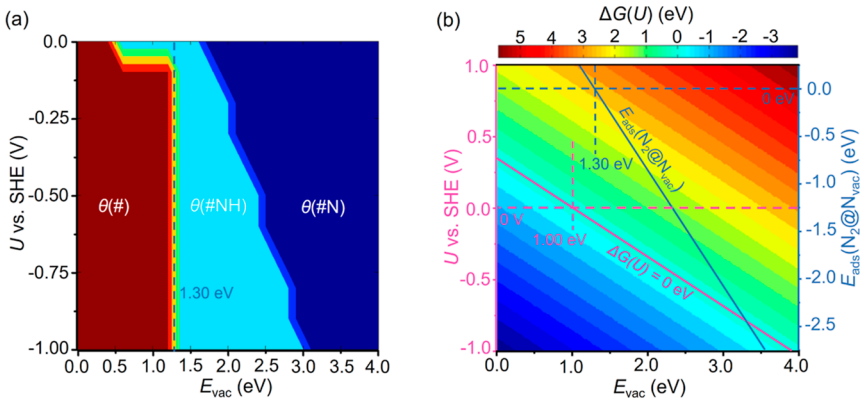

Figure 4. (a) Distribution diagram of main species on the surfaces of different MNs with change of E_{vac} and U, and the relative detailed coverage changes are shown in Figure S13. (b) Decomposition diagram of N_{lat} as a function of E_{vac} and applied potential U (vs SHE), where $\Delta G(U)$ is the Gibbs free energy change of N_{lat} leaching out at the potential U. $E_{ads}(N_2@N_{vac})$ is the adsorption energy of N_2 on N_{vac} of MN (100) surface.

a reliable descriptor for assessing their catalytic performance,[53−55] here we tested the formation energy of N_{vac} (E_{vac}) as a descriptor to express the energy information on each elementary step in NRR on different MNs.

From Figure S9a, one can find that the adsorption energies of N_2 on the metal site (M_{cus}) or N_{vac}, as well as the H adsorption energies on N_{lat}, have good linear correlations with E_{vac}

$$E_{ads}(N_2@M_{cus}) = -0.20E_{vac} + 0.03 \quad (1)$$

$$E_{ads}(N_2@N_{vac}) = -1.21E_{vac} + 1.58 \quad (2)$$

$$E_{ads}(H@N_{lat}) = 0.72E_{vac} - 1.76 \quad (3)$$

Significantly, a large E_{vac} is conducive to N_2 adsorption on both the M_{cus} and N_{vac} sites. Quantitatively, $E_{ads}(N_2@N_{vac})$ becomes more negative than $E_{ads}(N_2@M_{cus})$ when E_{vac} > 1.50 eV, demonstrating the superior N_2 activation ability of N_{vac} on the MNs with relatively high E_{vac}. In addition, it is noteworthy that N_2 and H species show the opposite variation trends; the larger E_{vac} enhances the adsorption ability toward N_2 but weakens the binding strength of H species on N_{lat}. As depicted in Figure S9b−e, the barriers and enthalpy changes of all elementary steps in either the L−H or MvK pathways exhibit linear scaling with E_{vac}. Almost all of these correlations have negative slopes, indicating that these steps become easier to proceed as E_{vac} increases. The primary cause of this phenomenon is the weaker H binding at N_{lat} and the stronger binding of the M_{cus} sites as E_{vac} increases. This facilitates the hydrogenation steps and N−N bond cleavage. Overall, an increase in E_{vac} is beneficial for activating the N_2 molecule, promoting the N_{lat}/N_2 hydrogenation and the N−N bond cleavage, while simultaneously weakening the H binding at the surface N_{lat} site. Therefore, E_{vac} proved to be an efficient indicator.

NRR Activity of MNs

Based on these scaling relations, we constructed the microkinetic model to inspect the NRR activity and stability trends at different working potentials and T = 300 K (see the microkinetic details in Note S4). In the microkinetic simulation, we also probed the NRR selectivity by incorporating the competitive HER (details in Note S5). Figure 3a illustrates the activity trend of different MNs for NRR by plotting the logarithms of turnover frequency (TOF) as a function of E_{vac} and working potential U (vs SHE). The NH_3 formation rates are proportional to E_{vac} and U. Specifically, MNs with a low E_{vac} (i.e., the highly reactive N_{lat}) consistently exhibit low catalytic activities. As E_{vac} increases, the corresponding catalytic activities gradually increase. However, when E_{vac} increases to a certain extent, N_{lat} becomes inert and the catalytic activity is severely limited; only when a high potential is applied can these MNs catalyze NRR again. Unfortunately, as demonstrated in Figure S11, the HER is progressively promoted at high potentials and yields a comparable rate of NH_3 formation on these high-E_{vac} MNs. This suggests a low selectivity of NRR at this stage, which is not desirable for the experiment. Therefore, to ensure the more favored formation of NH_3 rather than H_2, the optimal potential U for MNs should be controlled within a range of low potential (>−0.5 V). However, in such a situation, it corresponds to a very low maximum NH_3 formation rate of only ∼10^{-6} s^{-1} $site^{-1}$ (∼10^{-15} mol s^{-1} cm^{-2}) on MN(100).

To inspect the activity analysis of MN catalysts for NRR, a microkinetic simulation was conducted at the typical voltage U = −0.3 V (vs SHE). Two volcano-type activity curves following the L−H or MvK pathways were obtained. Figure 3b shows that the MvK pathway is generally more favored than the L−H pathway over a wide range, as evidenced by the fact that the MvK activity curve is overall higher than the L−H one and reaches a much higher maximum point. The L−H pathway becomes active only when E_{vac} increases to a certain extent (>3.20 eV), where N_{lat} is too inert to be reduced. For instance, NRR on CrN(100), VN(100), and TiN(100) predominantly follows the MvK pathway, while on ZrN(100) it follows the L−H pathway. This suggests that the MvK pathway is the primary route for NRR on MNs, which accords with the experimental reports.[17−26]

On analyzing the activity curve (Figure 3b), it is evident that it rises significantly from a low E_{vac} and reaches an inflection point at E_{vac} = 1.30 eV. In the range of E_{vac} < 1.30 eV, the rate-limiting step is the hydrogenation of $\#N_2$ ($\#N_2 \rightarrow \#NNH$), as indicated by the higher rate control sensitivity X_{RC} (Figure 3c). Combining with the coverage change (Figure 3d), the increased activity in this range is attributed to the decreased energy barrier and the rapidly increased coverage of N_2 on N_{vac} [$\theta(\#N_2)$] and H species on N_{lat} [$\theta(\#NH)$] with the increase of E_{vac}. After E_{vac} = 1.30 eV, the activity curve becomes flat and gradually reaches the maximum point at E_{vac} = 2.10 eV, which corresponds to an optimal NRR activity (but only ∼10^{-6} s^{-1} $site^{-1}$). In the range 1.30 eV < E_{vac} < 2.10 eV, the rate-limiting

https://doi.org/10.1021/jacsau.4c00377
JACS Au 2024, 4, 3038−3048

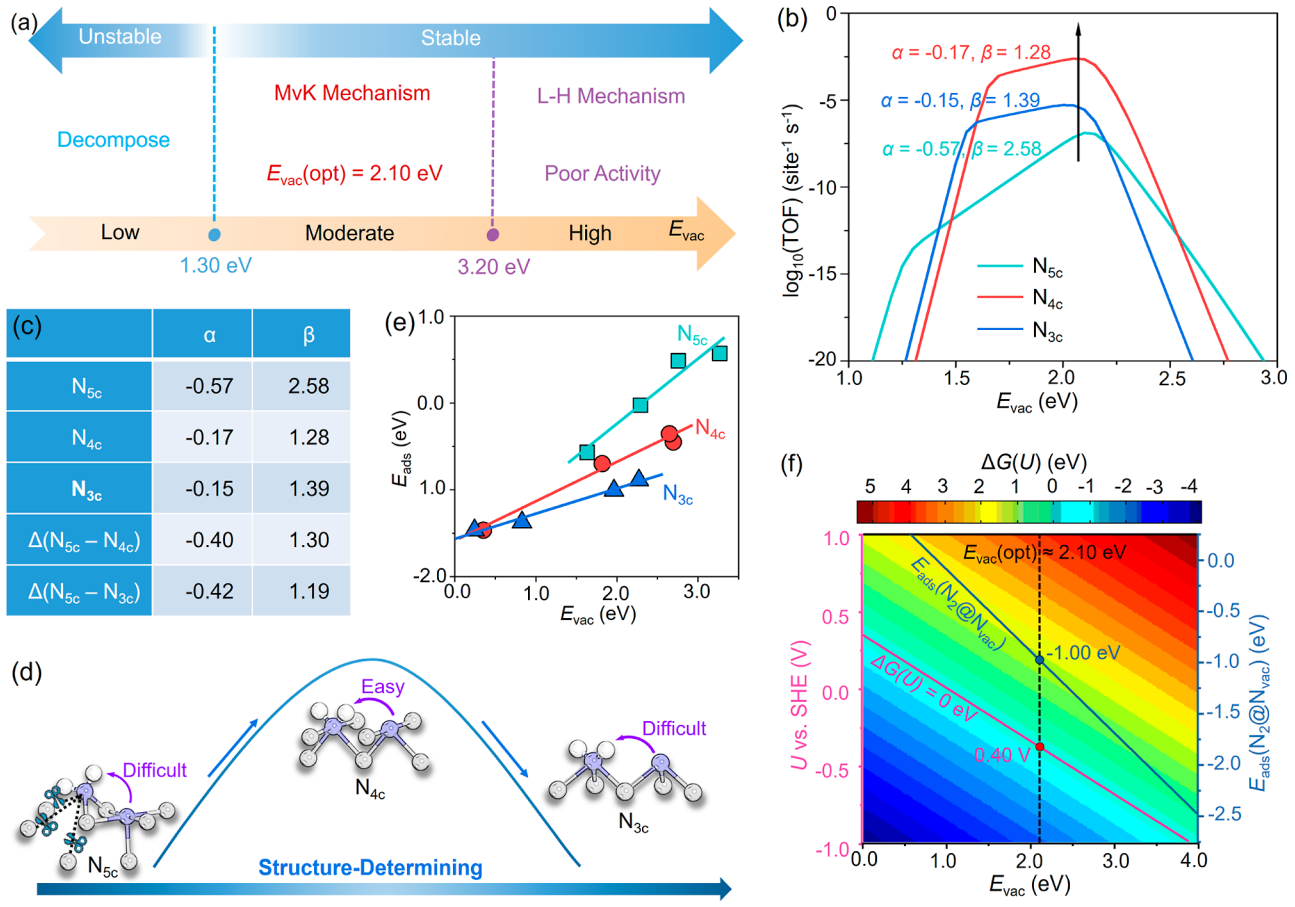

(c)	α	β
N_{5c}	-0.57	2.58
N_{4c}	-0.17	1.28
N_{3c}	-0.15	1.39
$\Delta(N_{5c} - N_{4c})$	-0.40	1.30
$\Delta(N_{5c} - N_{3c})$	-0.42	1.19

Figure 5. (a) Schematic diagram for rationally screening/designing the appropriate MN catalysts for NNR by E_{vac} at the low working potential. E_{vac}(opt) is the location of MNs with the optimum activity. (b) Schematic illustration of the influence of the scaling relation for the rate-limiting step #NH → #NH_2 on different structural N_{lat} on the peak height of the volcano-shaped activity curve. N_{5c}, N_{4c}, and N_{3c} represent the five-, four- and three-coordinate N_{lat}, respectively. (c) Slopes (α) and intercepts (β) of the relation for the rate-limiting step RLS-1 as a function of E_{vac} on different coordinate N_{lat}, respectively. (d) Structural features of N_{5c}, N_{4c}, and N_{3c}, and the corresponding activity changing trend. The white, blue, and gray balls represent the hydrogen, nitrogen and metal atoms, respectively. (e) Relationships of adsorption energies of H species on N_{5c}, N_{4c}, and N_{3c}, respectively. (f) Decomposition diagram of N_{lat} as a function of E_{vac} and applied potential U (vs SHE), where $\Delta G(U)$ is the Gibbs free energy change of N_{lat} leaching out at the potential U (vs SHE). $E_{ads}(N_2@N_{vac})$ is the adsorption energy of N_2 on N_{vac} of N_{4c}.

step changes from #N_2 hydrogenation to N_{lat}H hydrogenation (#NH → #NH_2, Figure 3c). When E_{vac} > 2.10 eV, the activity begins to decline rapidly, primarily due to the inert N_{lat} evidenced by θ(#N) ≈ 1 ML (Figure 3d). Specifically, CrN(100) and VN(100) were previously predicted to be efficient for NRR based on a simplified thermodynamic assessment;[24] however, despite being located around the optimal point of the activity curve, they exhibit a low reaction rate of only about 10^{-10} s^{-1} $site^{-1}$ (~10^{-19} mol s^{-1} cm^{-2}) under the quantitative microkinetic simulation. As can be seen from the activity curves, for MNs(100) with too reactive or too inert N_{lat}, adjusting E_{vac} to a moderate degree (~2.10 eV) can improve their catalytic activities for NNR; however, even at this optimal point, the catalytic activity remains limited, with a NH_3 formation rate of only ~10^{-6} s^{-1} $site^{-1}$ (~10^{-15} mol s^{-1} cm^{-2} $site^{-1}$, see the detailed discussions in the latter).

Electrochemical Stability of MNs

It is worth discussing that if consumed N_{lat} in the MvK pathway cannot be replenished in time, MNs would eventually decompose and lose catalytic activity. In other words, the competition between N_{lat} dissolution in the form of NH_3 and N_2 adsorption in N_{vac} could determine the stability of MNs in the realistic NRR environment. Quantitatively, the distribution diagram of the key species on different MNs(100) at the kinetic steady state was plotted as a function of E_{vac} and potential U by virtue of microkinetic simulation (Figure 4a), which can provide an explicit description of the surface environment.

Figure 4a shows that on MNs with low E_{vac} (<1.30 eV), the coverage of N_{vac} [θ(#)] is almost 1 ML at typical potentials, demonstrating that the surface N_{lat} has been leached out at the steady state. Therefore, these MNs tend to decompose and are unsuitable for catalyzing NRR. The electrochemical phase diagram of MN(100) surfaces (Figure 4b), which describes the Gibbs free energy change [$\Delta G(U)$] of the N_{lat} leaching-out process (details in Note S6), can rationalize the origin of the low stability of these MNs. As Figure 4b shows, when MN(100) has low E_{vac} (<1.00 eV), the dissolution U is larger than 0 eV, indicating that this surface N_{lat} would be reduced to NH_3 and released easily even at the very small reduction potential. At the same time, the low E_{vac} means the weak N_2 adsorption on N_{vac} (Figure S9a), and $E_{ads}(N_2@N_{vac})$ is even positive (>0.55 eV), implying the difficult supply of N_2 on N_{vac}. As E_{vac} > 1.00 eV, although the dissolution U begins to become negative, $E_{ads}(N_2@N_{vac})$ is still larger than 0 eV until E_{vac} = 1.30 eV, and therefore the MNs would still be unstable at the

https://doi.org/10.1021/jacsau.4c00377
JACS Au 2024, 4, 3038−3048

usual low reduction potential due to the difficult supply of N_2 to fill N_{vac}. When E_{vac} is above 1.30 eV, the microkinetic results show that the N_{vac} coverage gradually decreases, and the surface N_{lat} coverage increases at the steady state; at this time, the N_2 supply also becomes thermodynamically favored and can compete with the decomposition of N_{lat}, as illustrated in Figure 4a,b.

In general, for MNs with low E_{vac}, the insufficient adsorption of N_2 cannot balance the N_{lat} release, leading to abundant N_{vac} on these metal-nitride surfaces and catalyst deactivation. This explains the phenomenon that NH_3 formation occurs only at the preliminary stage on some MNs and decreases quickly or is even undetectable over time.[36,37] The electrochemical stability of MNs can be improved as E_{vac} becomes higher. Based on these findings, it is worthwhile at this point to discuss the controversy on the stability of VN catalyst. (100) as the most stable surface of VN catalyst has an E_{vac} of 2.29 eV (>1.30 eV) and $E_{ads}(N_2@N_{vac})$ is strong (−0.96 eV), indicating its relative stability in the electrochemical NRR condition. In contrast, the VN(311) surface (taken as an example of secondarily exposed surfaces of VN catalyst) corresponds to an E_{vac} of only 0.73 eV and $E_{ads}(N_2@N_{vac})$ is limited by −0.33 eV, which implies that N_{lat} on the (311) surface could be easily reduced to NH_3 and released even at the low reduction potential based on the decomposition diagram of N_{lat} (Figure 4b), and thus, VN(311) is less stable. Therefore, the electrochemical stability of the VN catalyst in NRR could be critically determined by the exposed morphology during catalyst preparation, which may rationalize the different experimental observations on the stability of VN catalyst.[20−24,37]

Further Discussion on Designing MN for NRR

Overall, by integrating the above stability and activity analysis, a quantitative rule can be provided to assess the suitability of MNs for NRR. As illustrated in Figure 5a, MN(100) with low E_{vac} (<1.30 eV) is always unstable due to the easy reduction of N_{lat} and poor N_2 supply on N_{vac}, resulting in very low catalytic ability for NRR. When E_{vac} > 1.30 eV, MN(100) gradually favors the N_2 supply on N_{vac} and leads to improved catalytic activities and electrochemical stabilities. However, beyond a specific E_{vac} threshold, the catalytic activities decrease quickly due to the inert N_{lat}, despite excellent stabilities of these MNs at this time.

Nonetheless, it is essential to note that such a maximum reaction rate ($\sim 10^{-6}$ s^{-1} $site^{-1}$) on the (100) surface of rocksalt-type MNs falls below the demand for industrial application. To further improve the catalytic activity, increasing the electrode potential U could certainly be a possible strategy. As Figure 3a shows, the optimal NRR rate can reach 10^{-1} to 10^{0} s^{-1} $site^{-1}$ on high-E_{vac} rocksalt-type MNs (around E_{vac} = 2.80 eV) at the higher potential U = −0.8 V; however, at this time, HER would be improved even more and leads to a low NRR selectivity (Figure S11b). Therefore, elevating the electrode potential could not be a good method to improve the catalytic activity of MNs for NRR; increasing the intrinsic catalytic activity of MNs is crucial to overcome the limitations of the peak height of the volcano activity curve. To this end, it is a requisite to understand the inherent constraint on rocksalt-MN(100) catalysts. From the microkinetic analysis above, it can be seen that the peak position [E_{vac}(opt)] of the activity curve for rocksalt-MN(100) is largely determined by the intersection of two rate-limiting steps (RLS-1: #NH → #NH_2 and RLS-2: #NH_2 → #NH_3). Quantitatively, the peak height (r_{max}) can be expressed with reference to RLS-1

$$r_{max} = \frac{k_B T}{h} \exp\left(\frac{-\alpha E_{vac}(\text{opt}) - \beta}{k_B T}\right) \times \theta(\#\text{NH})^2 \quad (4)$$

where α and β are the slope and intercept, respectively, of the linear correlation of the barrier of RLS-1 as a function of E_{vac}. E_{vac}(opt) is the peak position of the activity curve, around 2.10 eV. θ(#NH) is the coverage of H species on N_{lat}, which is nearly 1 ML at E_{vac}(opt) (Figure 3d). Hence, r_{max} can be simplified as being directly proportional to α and β

$$\ln r_{max} \propto -\alpha E_{vac}(\text{opt}) - \beta \quad (5)$$

Accordingly, slope α and intercept β are the critical factors influencing r_{max}. Since these two parameters are constant for the catalysts of the same structural type,[56,57] it can be speculated that breaking the scaling relationship limit of α and β on the five-coordinate N_{lat} (denoted as N_{5c}) of MNs(100) may be an effective strategy to enhance their intrinsic catalytic activity.

To verify this hypothesis, we explored the barriers of RLS-1 on the four- (or three-) coordinate N_{lat} (denoted as N_{4c} and N_{3c}, respectively), on the other low Miller index (110) and (111) surfaces of rock-salt-type MNs as a proof of concept. After scaling these barriers and enthalpy changes on N_{4c} and N_{3c} with E_{vac}, we can establish new relations (Figure S14) and the higher r_{max} can be obtained around E_{vac} = 2.10 eV (r_{max}: N_{4c} > N_{3c} > N_{5c}); especially, there is a r_{max} as high as 10^{-2} s^{-1} $site^{-1}$ on N_{4c} ($\sim 10^{-11}$ mol s^{-1} cm^{-2}, Figure 5b), which is about 10^4 times larger than that on N_{5c}. Compared with N_{5c} (Figure 5c), the slope α on N_{4c} and N_{3c} decreases but the difference in α values is relatively small; by comparison, the β term on N_{4c} and N_{3c} is much lower than that on N_{5c} (1.28/1.39 eV vs 2.58 eV). In other words, the larger r_{max} on N_{4c} and N_{3c} can be attributed to the much smaller β term, which can decrease the overall energy barrier of N_{lat} hydrogenation and facilitate NRR.

The intercept β is determined by the local structural features of active sites.[56−58] In terms of the rate-determining #NH_2 formation step ($N_{lat}H + N_{lat}H \rightarrow N_{lat}H_2 + N_{lat}$), there are two main factors affecting this H transfer process: (i) the cleavage of H−N_{lat} bond and (ii) the formation of new H−N_{lat}H bond with the possible cleavage of metal−nitrogen (M−N_{lat}) bonds accompanied on the catalyst surface. As shown in Figure 5d, one can see that the lattice N_{5c} is relatively saturated, which will become oversaturated as #NH_2 forms; thus, three M−N_{lat} bonds around N_{5c} are necessary to be broken and the N_{5c} is pulled out in NH_2 formation. Although the H adsorption on N_{5c} is relatively weaker compared with that on N_{4c} and N_{3c} (Figure 5e), these three M−N_{lat} bonds are relatively difficult to break, thus leading to higher β; the higher β indicates that the rate-determining #NH_2 formation on N_{5c} is more difficult. By comparison, on the tapered N_{3c}, the lattice N_{lat} becomes five-coordinated as #NH_2 forms, which is still relatively unsaturated compared to the most stable six-coordinate N_{lat} in the bulk phase. Thus, #NH_2 can be stabilized without breaking any M−N_{lat} bond. However, the H adsorption on N_{3c} is much stronger than that on N_{5c} (Figure 5e), which limits the H transfer to some extent. For the most promoted N_{4c}, it can basically stay at the original lattice position with a stable six-coordination configuration during the #NH_2 formation process, which is the most stable structure for N_{lat} in MN and does not need to break any M−N_{lat} bond. In addition, N_{4c} exhibits an edge

https://doi.org/10.1021/jacsau.4c00377
JACS Au 2024, 4, 3038−3048

structure and has a moderate H adsorption strength that is relatively weaker than that of the tapered N_{3c} (Figure 5e). Thus, the H transfer between N_{4c} is more favorable compared with that between N_{3c}, resulting in the lowest β and contributing to the largest r_{max} for NRR (Figure 5b).

Noteworthily, according to the decomposition diagram of N_{lat} (as a function of E_{vac} and applied potential U; see Figure 5f), one can see that for N_{lat} at $E_{vac}(opt) \approx 2.10$ eV, the tolerate potential U can reach −0.4 V vs SHE, implying that only when the reduction potential U is more negative than −0.4 V, these N_{4c} would tend to decompose in the form of NH_3 energetically. In addition, in the N_{4c} vacancy site at $E_{vac}(opt) \approx 2.10$ eV, the N_2 adsorption is strong with $E_{ads}(N_2@N_{vac})$ being −1.0 eV. It is therefore expected that the N_{4c} configuration is stable under the reaction condition of NRR with a relatively small applied potential ($U > -0.4$ V) that is generally used in the experiment. In other words, N_{4c} could be an important topology of N_{lat} for NRR, which can achieve a win−win in terms of activity and stability.

CONCLUSIONS

In summary, this work reported a systematic investigation into the electrocatalytic NRR on MNs, in which the molecular-level mechanism of NRR was identified, and structure−activity−stability maps of NRR on different metal-nitrides were established by the microkinetic simulations. Mechanically, we verified that the MvK pathway is kinetically more favorable to drive NRR on a majority of MNs, where N_{lat} plays a pivotal role in achieving the Volmer process and N_2 activation; only on MNs with inert N_{lat}, the L−H pathway works. More importantly, we quantitatively revealed the stability, activity, and selectivity trends of MNs for NRR, which closely depend on E_{vac}. MNs with low E_{vac} are unstable and easily decompose, and are incapable of activating N_2 efficiently. The high-E_{vac} ones give low catalytic activities despite superior electrochemical stabilities; only at the elevated potential, they could achieve improved NRR activities but encounter low selectivity (vs HER). The moderate-E_{vac} MNs can give the maximum activity and keep good electrochemical stability; this activity maximum is, however, largely limited with the NH_3 yield of only $\sim 10^{-6}$ s^{-1} $site^{-1}$ ($\sim 10^{-15}$ mol s^{-1} cm^{-2}) owing to the structural feature of five-coordinate N_{lat} on rocksalt-type MN(100). To break through this activity limitation, we explored the activity-regulating role of the local structural features of N_{lat}, and we proposed that surface engineering by adopting the fine local structures of N_{lat} (e.g., four-coordinate N_{lat}, $E_{vac}(opt) \approx 2.10$ eV) on MNs could potentially improve the NH_3 yield up to an anticipated $\sim 10^{-2}$ s^{-1} $site^{-1}$ in experiments. We believe that this work provides an in-depth insight into NRR on MNs and theoretically illustrates whether/how MNs can be suitable for NRR. These fundamental understandings offer direction to design or optimize metal-nitride catalysts.

METHODS

Calculation Method

All spin-polarized density functional theory (DFT) calculations were performed by VASP,[59] using the Perdew−Burke−Ernzerhof functional within the generalized gradient approximation.[60] The core−valence electron interaction was described by the project-augmented wave method,[61] and the valence electronic states were expanded in the plane wave basis sets with an energy cutoff of 450 eV. Van der Waals dispersion (DFT-D3) was included, and the DFT + U approach with the on-site coulomb correction included was used to describe the localized 3d-orbital of V element (U_{eff} = 3.0 eV).[62,63] The geometries were optimized by using the Broyden method until the maximal force on each relaxed atom was less than 0.05 eV/Å. The rocksalt-type MN (100) surface was described with a $p(2 \times 2)$ slab with five atomic layers. During structural optimization, the bottom two layers of the slab were fixed, the top three layers and adsorbates were fully relaxed, and the vacuum between slabs was set to 15 Å; a $3 \times 3 \times 1$ k-point mesh was used. The constrained optimization method was used to search the transition state, which has been widely verified.[64,65] The microkinetic simulation was carried out with the CATKINAS package.[66−69] The formation energy (E_{vac}) of the nitrogen vacancy was calculated with the following equation: $E_{vac} = (E_{sur\_vac} + 1/2E_{N_2}) - E_{sur}$, where E_{sur} and E_{sur_vac} are the total energies of the pristine surface and surface with one nitrogen vacancy, and E_{N_2} is the total energy of N_2 molecule, respectively.

EFFECT OF POTENTIAL AND SOLVENT

For the process involving the proton−electron pair (H^+/e^-), the reaction free energy was calculated by using the computational hydrogen electrode model (CHE). In this approach, the chemical potential of H^+/e^- is equilibrated with half the free energy of an H_2 molecule at 0 V (vs SHE), while the effect of external potential U was accounted for by including the $-eU$ correction.[70,71] The potential dependent reaction barrier at a constant potential was calculated by the charge-extrapolation method (see the details in Note S1).[72−74] Notably, with respect to the solvent-induced stabilization effect toward the NRR-related adsorbates, it has been estimated to be comparatively small, and contributes little to the tendency judgment.[50,51] To further illustrate the influence of solvation energy in our system, we chose the N_2 and N_{lat} hydrogenation steps ($*N_2 + N_{lat}H \rightarrow *NNH + N_{lat}$ and $N_{lat}H \rightarrow N_{lat}H_2$) at the water/VN(100) interface as examples and calculated its energy barrier and reaction energy in explicit water by performing the multipoint averaging molecular dynamics (MPA-MD).[52] It shows that the difference with and without a water environment is reliably small (Table S2), ∼0.20 eV, demonstrating again a relatively small effect on judging the activity trend. Herein, our DFT calculations were mainly conducted on the bare surfaces by balancing the too-heavy ab Initio molecular dynamics simulations for each elementary step occurring on the catalyst surface.

ASSOCIATED CONTENT

Supporting Information

The Supporting Information is available free of charge at https://pubs.acs.org/doi/10.1021/jacsau.4c00377.

Detailed reaction pathway of the L−H and MvK mechanisms on VN(100), H_2 evolution reaction information on VN(100), and TS or intermediate structures, and microkinetic details and some related kinetic data (PDF)

AUTHOR INFORMATION

Corresponding Author

Haifeng Wang − *State Key Laboratory of Green Chemical Engineering and Industrial Catalysis, Center for Computational Chemistry and Research Institute of Industrial Catalysis, School of Chemistry and Molecular Engineering, East China University of Science and*

https://doi.org/10.1021/jacsau.4c00377
JACS Au 2024, 4, 3038−3048

Technology, Shanghai 200237, China; orcid.org/0000-0002-6138-5800; Email: hfwang@ecust.edu.cn

Authors

Haiyang Yuan − *Key Laboratory for Ultrafine Materials of Ministry of Education, Shanghai Engineering Research Center of Hierarchical Nanomaterials, School of Materials Science and Engineering, East China University of Science and Technology, Shanghai 200237, China;* orcid.org/0000-0001-6175-391X

Chen Zhu − *Key Laboratory for Ultrafine Materials of Ministry of Education, Shanghai Engineering Research Center of Hierarchical Nanomaterials, School of Materials Science and Engineering, East China University of Science and Technology, Shanghai 200237, China*

Yu Hou − *Key Laboratory for Ultrafine Materials of Ministry of Education, Shanghai Engineering Research Center of Hierarchical Nanomaterials, School of Materials Science and Engineering, East China University of Science and Technology, Shanghai 200237, China;* orcid.org/0000-0003-1691-7561

Hua Gui Yang − *Key Laboratory for Ultrafine Materials of Ministry of Education, Shanghai Engineering Research Center of Hierarchical Nanomaterials, School of Materials Science and Engineering, East China University of Science and Technology, Shanghai 200237, China;* orcid.org/0000-0003-0436-8622

Complete contact information is available at: https://pubs.acs.org/10.1021/jacsau.4c00377

Author Contributions

H. W. directed this project. H. Y. performed the DFT calculations, data analyses, and wrote the manuscript. C. Z. gave the assistance with some DFT calculations and data analyses. Y. H. and H. G. Y. gave helpful suggestions for the research. All the authors participated in writing and editing the manuscript and contributed their efforts to the discussion. CRediT: **Haiyang Yuan** conceptualization, data curation, formal analysis, funding acquisition, investigation, writing-original draft, writing-review & editing; **Chen Zhu** data curation, formal analysis, investigation; **Yu Hou** writing-review & editing; **Hua Gui Yang** writing-review & editing; **Haifeng Wang** conceptualization, formal analysis, funding acquisition, methodology, project administration, supervision, writing-review & editing.

Notes

The authors declare no competing financial interest.

■ ACKNOWLEDGMENTS

This work was supported by the National Key Research and Development Program of China (2021YFA1500700), the Science and Technology Commission of Shanghai Municipality (23ZR1416800), and the Fundamental Research Funds for the Central Universities.

■ REFERENCES

(1) Brown, K. A.; Harris, D. F.; Wilker, M. B.; Rasmussen, A.; Khadka, N.; Hamby, H.; Keable, S.; Dukovic, G.; Peters, J. W.; Seefeldt, L. C.; King, P. W. Light-Driven Dinitrogen Reduction Catalyzed by a CdS: Nitrogenase MoFe Protein Biohybrid. *Science* **2016**, *352*, 448−450.

(2) van Kessel, M. A.; Speth, D. R.; Albertsen, M.; Nielsen, P. H.; Op den Camp, H. J. M.; Kartal, B.; Jetten, M. S.; Lücker, S. Complete Nitrification by a Single Microorganism. *Nature* **2015**, *528*, 555−559.

(3) Canfield, D. E.; Glazer, A. N.; Falkowski, P. G. The Evolution and Future of Earth's Nitrogen Cycle. *Science* **2010**, *330*, 192−196.

(4) Klerke, A.; Christensen, C. H.; Nørskov, J. K.; Vegge, T. Ammonia for Hydrogen Storage: Challenges and Opportunities. *J. Mater. Chem.* **2008**, *18*, 2304−2310.

(5) Liu, J. C.; Ma, X. L.; Li, Y.; Wang, Y. G.; Xiao, H.; Li, J. Heterogeneous Fe_3 Single-Cluster Catalyst for Ammonia Synthesis via an Associative Mechanism. *Nat. Commun.* **2018**, *9*, 1610−1619.

(6) Foster, S. L.; Bakovic, S. I. P.; Duda, R. D.; Maheshwari, S.; Milton, R. D.; Minteer, S. D.; Janik, M. J.; Renner, J. N.; Greenlee, L. F. Catalysts for Nitrogen Reduction to Ammonia. *Nat. Catal.* **2018**, *1*, 490−500.

(7) Chirik, P. J. Nitrogen Fixation: One Electron at A Time. *Nat. Chem.* **2009**, *1*, 520−522.

(8) Murakami, T.; Nishikiori, T.; Nohira, T.; Ito, Y. Electrolytic Synthesis of Ammonia in Molten Salts under Atmospheric Pressure. *J. Am. Chem. Soc.* **2003**, *125*, 334−335.

(9) Suryanto, B. H.; Du, H. L.; Wang, D.; Chen, J.; Simonov, A. N.; MacFarlane, D. R. Challenges and Prospects in the Catalysis of Electroreduction of Nitrogen to Ammonia. *Nat. Catal.* **2019**, *2*, 290−296.

(10) Chen, Y.; Liu, H.; Ha, N.; Licht, S.; Gu, S.; Li, W. Revealing Nitrogen-Containing species in Commercial Catalysts Used for Ammonia Electrosynthesis. *Nat. Catal.* **2020**, *3*, 1055−1061.

(11) Li, K.; Andersen, S. Z.; Statt, M. J.; Saccoccio, M.; Bukas, V. J.; Krempl, K.; Sažinas, R.; Pedersen, J. B.; Shadravan, V.; Zhou, Y.; Chakraborty, D.; Kibsgaard, J.; Vesborg, P. C. K.; Nørskov, J. K.; Chorkendorff, I. Enhancement of Lithium-Mediated Ammonia Synthesis by Addition of Oxygen. *Science* **2021**, *374*, 1593−1597.

(12) Du, H. L.; Chatti, M.; Hodgetts, R. Y.; Cherepanov, P. V.; Nguyen, C. K.; Matuszek, K.; MacFarlane, D. R.; Simonov, A. N. Electroreduction of Nitrogen with Almost 100% Current-to-ammonia Efficiency. *Nature* **2022**, *609*, 722−727.

(13) Zhang, S.; Han, M.; Shi, T.; Zhang, H.; Lin, Y.; Zheng, X.; Zheng, L. R.; Zhou, H.; Chen, C.; Zhang, Y.; Wang, G.; Yin, H.; Zhao, H. Atomically Dispersed Bimetallic Fe-Co Electrocatalysts for Green Production of Ammonia. *Nat. Sustain.* **2022**, *6*, 169−179.

(14) Cai, W.; Jiang, Y. F.; Zhang, J.; Yang, H.; Zhang, J.; Xu, C. Q.; Liu, W.; Li, J.; Liu, B. Ruthenium/Titanium Oxide Interface Promoted Electrochemical Nitrogen Reduction Reaction. *Chem Catal.* **2022**, *2*, 1764−1774.

(15) Li, S.; Bao, D.; Shi, M.; Wulan, B.; Yan, J.; Jiang, Q. Amorphizing of Au Nanoparticles by CeO_x-RGO Hybrid Support towards Highly Efficient Electrocatalyst for N_2 Reduction under Ambient Conditions. *Adv. Mater.* **2017**, *29*, 1700001.

(16) Hao, Y. C.; Guo, Y.; Chen, L. W.; Shu, M.; Wang, X. Y.; Bu, T. A.; Gao, W. Y.; Zhang, N.; Su, X.; Feng, X.; Zhou, J. W.; Wang, B.; Hu, C. W.; Yin, A. X.; Si, R.; Zhang, Y. W.; Yan, C. H. Promoting Nitrogen Electroreduction to Ammonia with Bismuth Nanocrystals and Potassium Cations in Water. *Nat. Catal.* **2019**, *2*, 382−384.

(17) Li, Q.; He, L.; Sun, C.; Zhang, X. Computational Study of MoN_2 Monolayer as Electrochemical Catalysts for Nitrogen Reduction. *J. Phys. Chem. C* **2017**, *121*, 27563−27568.

(18) Zeinalipour-Yazdi, C. D.; Hargreaves, J. S.; Catlow, C. R. A. Nitrogen Activation in a Mars-van Krevelen Mechanism for Ammonia Synthesis on Co_3Mo_3N. *J. Phys. Chem. C* **2015**, *119*, 28368−28376.

(19) Qiao, Z.; Johnson, D.; Djire, A. Challenges and Opportunities for Nitrogen Reduction to Ammonia on Transitional Metal Nitrides via Mars-van Krevelen Mechanism. *Cell Rep. Phys. Sci.* **2021**, *2*, 100438.

(20) Yang, X.; Kattel, S.; Nash, J.; Chang, X.; Lee, J. H.; Yan, Y.; Chen, J. G.; Xu, B. Quantification of Active Sites and Elucidation of the Reaction Mechanism of the Electrochemical Nitrogen Reduction Reaction on Vanadium Nitride. *Angew. Chem.* **2019**, *131*, 13906−13910.

(21) Yang, X.; Nash, J.; Anibal, J.; Dunwell, M.; Kattel, S.; Stavitski, E.; Attenkofer, K.; Chen, J. G.; Yan, Y.; Xu, B. Mechanistic Insights into Electrochemical Nitrogen Reduction Reaction on Vanadium Nitride Nanoparticles. *J. Am. Chem. Soc.* **2018**, *140*, 13387−13391.
(22) Zhang, R.; Zhang, Y.; Ren, X.; Cui, G.; Asiri, A. M.; Zheng, B.; Sun, X. High-Efficiency Electrosynthesis of Ammonia with High Selectivity under Ambient Conditions Enabled by VN Nanosheet Array. *ACS Sustainable Chem. Eng.* **2018**, *6*, 9545−9549.
(23) Zhang, X.; Kong, R. M.; Du, H.; Xia, L.; Qu, F. Highly Efficient Electrochemical Ammonia Synthesis via Nitrogen Reduction Reactions on a VN Nanowire Array under Ambient Conditions. *Chem. Commun.* **2018**, *54*, 5323−5325.
(24) Abghoui, Y.; Garden, A. L.; Howalt, J. G.; Vegge, T.; Skúlason, E. Electroreduction of N_2 to Ammonia at Ambient Conditions on Mononitrides of Zr, Nb, Cr, and V: A DFT Guide for Experiments. *ACS Catal.* **2016**, *6*, 635−646.
(25) Zhang, L.; Ji, X.; Ren, X.; Luo, Y.; Shi, X.; Asiri, A. M.; Zheng, B.; Sun, X. Efficient Electrochemical N_2 reduction to NH_3 on MoN Nanosheets Array under Ambient Conditions. *ACS Sustain. Chem. Eng.* **2018**, *6*, 9550−9554.
(26) Ren, X.; Cui, G.; Chen, L.; Xie, F.; Wei, Q.; Tian, Z.; Sun, X. Electrochemical N_2 Fixation to NH_3 under Ambient Conditions: Mo_2N Nanorod as a Highly Efficient and Selective Catalyst. *Chem. Commun.* **2018**, *54*, 8474−8477.
(27) Liu, X.; Jiao, Y.; Zheng, Y.; Jaroniec, M.; Qiao, S. Z. Building up a Picture of the Electrocatalytic Nitrogen Reduction Activity of Transition Metal Single-Atom Catalysts. *J. Am. Chem. Soc.* **2019**, *141*, 9664−9672.
(28) Geng, Z.; Liu, Y.; Kong, X.; Li, P.; Li, K.; Liu, Z.; Du, J.; Shu, M.; Si, R.; Zeng, J. Achieving a Record-High Yield Rate of 120.9 for N_2 Electrochemical Reduction over Ru Single-Atom Catalysts. *Adv. Mater.* **2018**, *30*, 1803498.
(29) Zhao, J.; Chen, Z. Single Mo Atom Supported on Defective Boron Nitride Monolayer as an Efficient Electrocatalyst for Nitrogen Fixation: A Computational Study. *J. Am. Chem. Soc.* **2017**, *139*, 12480−12487.
(30) Liu, C.; Li, Q.; Wu, C.; Zhang, J.; Jin, Y.; MacFarlane, D. R.; Sun, C. Single-Boron Catalysts for Nitrogen Reduction Reaction. *J. Am. Chem. Soc.* **2019**, *141*, 2884−2888.
(31) Andersen, S. Z.; Čolić, V.; Yang, S.; Schwalbe, J. A.; Nielander, A. C.; McEnaney, J. M.; Enemark-Rasmussen, K.; Baker, J. G.; Singh, A. R.; Rohr, B. A.; Statt, M. J.; Blair, S. J.; Mezzavilla, S.; Kibsgaard, J.; Vesborg, P. C. K.; Cargnello, M.; Bent, S. F.; Jaramillo, T. F.; Stephens, I. E. L.; Nørskov, J. K.; Chorkendorff, I. A Rigorous Electrochemical Ammonia Synthesis Protocol with Quantitative Isotope Measurements. *Nature* **2019**, *570*, 504−508.
(32) Kibsgaard, J.; Nørskov, J. K.; Chorkendorff, I. The Difficulty of Proving Electrochemical Ammonia Synthesis. *ACS Energy Lett.* **2019**, *4*, 2986−2988.
(33) Choi, J.; Suryanto, B. H. R.; Wang, D.; Du, H. L.; Hodgetts, R. Y.; Ferrero Vallana, F. M.; MacFarlane, D. R.; Simonov, A. N. Identification and Elimination of False Positives in Electrochemical Nitrogen Reduction Studies. *Nat. Commun.* **2020**, *11*, 5546−5610.
(34) Ye, T. N.; Park, S. W.; Lu, Y.; Li, J.; Sasase, M.; Kitano, M.; Tada, T.; Hosono, H. Vacancy-enabled N_2 Activation for Ammonia Synthesis on an Ni-loaded Catalyst. *Nature* **2020**, *583*, 391−395.
(35) Ye, T. N.; Park, S. W.; Lu, Y.; Li, J.; Sasase, M.; Kitano, M.; Hosono, H. Contribution of Nitrogen Vacancies to Ammonia Synthesis over Metal Nitride Catalysts. *J. Am. Chem. Soc.* **2020**, *142*, 14374−14383.
(36) Du, H. L.; Gengenbach, T. R.; Hodgetts, R.; MacFarlane, D. R.; Simonov, A. N. Critical Assessment of the Electrocatalytic Activity of Vanadium and Niobium Nitrides toward Dinitrogen Reduction to Ammonia. *ACS Sustainable Chem. Eng.* **2019**, *7*, 6839−6850.
(37) Manjunatha, R.; Karajić, A.; Teller, H.; Nicoara, K.; Schechter, A. Electrochemical and Chemical Instability of Vanadium Nitride in the Synthesis of Ammonia Directly from Nitrogen. *ChemCatChem* **2020**, *12*, 438−443.
(38) Hanifpour, F.; Canales, C. P.; Fridriksson, E. G.; Sveinbjörnsson, A.; Tryggvason, T. K.; Yang, J.; Arthur, C.; Jónsdóttir, S.; Garden, A. L.; Ólafsson, S.; Leósson, K.; Árnadóttir, L.; Lewin, E.; Abghoui, Y.; Ingason, Á. S.; Magnus, F.; Flosadóttir, H. D.; Skúlason, E. Operando Quantification of Ammonia Produced from Computationally-Derived Transition Metal Nitride Electrocatalysts. *J. Catal.* **2022**, *413*, 956−967.
(39) Hu, B.; Hu, M.; Seefeldt, L.; Liu, T. L. Electrochemical Dinitrogen Reduction to Ammonia by Mo_2N: Catalysis or Decomposition? *ACS Energy Lett.* **2019**, *4*, 1053−1054.
(40) Bondarchuk, O.; Morel, A.; Belanger, D.; Goikolea, E.; Brousse, T.; Mysyk, R. Thin Films of Pure Vanadium Nitride: Evidence for Anomalous Non-faradaic Capacitance. *J. Power Sources* **2016**, *324*, 439−446.
(41) Huang, T.; Mao, S.; Zhou, G.; Wen, Z.; Huang, X.; Ci, S.; Chen, J. Hydrothermal Synthesis of Vanadium Nitride and Modulation of Its Catalytic Performance for Oxygen Reduction Reaction. *Nanoscale* **2014**, *6*, 9608−9613.
(42) Iqbal, A.; Skulason, E.; Abghoui, Y. Electrochemical Nitrogen Reduction to Ammonia at Ambient Condition on the (111) Facets of Transition Metal Carbonitrides. *ChemPhysChem* **2024**, *25*, No. e202300991.
(43) Abghoui, Y.; Iqbal, A.; Skulason, E. The Role of Overlayered Nitride Electro-materials for N_2 Reduction to Ammonia. *Front. Catal.* **2023**, *2*, 1096824.
(44) Iqbal, A.; Skulason, E.; Abghoui, Y. Are (100) Facets of Transition Metal Carbonitrides Suitable as Electrocatalysts for Nitrogen Reduction to Ammonia at Ambient Conditions. *Int. J. Hydrogen Energy* **2024**, *64*, 744−753.
(45) Ellingsson, V.; Iqbal, A.; Skulason, E.; Abghoui, Y. Nitrogen Reduction Reaction to Ammonia on Transition Metal Carbide Catalysts. *ChemSusChem* **2023**, *16*, No. e202300947.
(46) Lou, Z.; Zhou, S.; Hou, Y.; Yang, H. G.; Yuan, H.; Wang, H. High-Throughput Screening of Metal Nitrides for Electrochemical Nitrogen Reduction. *Appl. Surf. Sci.* **2024**, *665*, 160289.
(47) Montoya, J. H.; Tsai, C.; Vojvodic, A.; Nørskov, J. K. The Challenge of Electrochemical Ammonia Synthesis: A New Perspective on the Role of Nitrogen Scaling Relations. *ChemSusChem* **2015**, *8*, 2180−2186.
(48) Abghoui, Y.; Skúlason, E. Computational Predictions of Catalytic Activity of Zincblende (110) Surfaces of Metal Nitrides for Electrochemical Ammonia Synthesis. *J. Phys. Chem. C* **2017**, *121*, 6141−6151.
(49) Li, H.; Guo, S.; Shin, K.; Wong, M. S.; Henkelman, G. Design of a Pd−Au Nitrite Reduction Catalyst by Identifying and Optimizing Active Ensembles. *ACS Catal.* **2019**, *9*, 7957−7966.
(50) Abghoui, Y.; Skúlason, E. Electrochemical Synthesis of Ammonia via Mars-van Krevelen Mechanism on the (111) Facets of Group III-VII Transition Metal Mononitrides. *Catal. Today* **2017**, *286*, 78−84.
(51) Skúlason, E.; Bligaard, T.; Gudmundsdottir, S.; Studt, F.; Rossmeisl, J.; Abild-Pedersen, F.; Vegge, T.; Jónsson, H.; Nørskov, J. K. A Theoretical Evaluation of Possible Transition Metal Electrocatalysts for N_2 Reduction. *Phys. Chem. Chem. Phys.* **2012**, *14*, 1235−1245.
(52) Wang, D.; Sheng, T.; Chen, J.; Wang, H.; Hu, P. Identifying the Key Obstacle in Photocatalytic Oxygen Evolution on Rutile TiO_2. *Nat. Catal.* **2018**, *1*, 291−299.
(53) Yuan, H.; Sun, N.; Chen, J.; Jin, J.; Wang, H.; Hu, P. Insight into the NH_3-assisted Selective Catalytic Reduction of NO on β-MnO_2(110): Reaction Mechanism, Activity Descriptor and Evolution from the Pristine State to Steady State. *ACS Catal.* **2018**, *8*, 9269−9279.
(54) Yuan, H.; Chen, J.; Guo, Y.; Wang, H.; Hu, P. Insight into the Superior Catalytic Activity of MnO_2 for Low-Content NO Oxidation at Room Temperature. *J. Phys. Chem. C* **2018**, *122*, 25365−25373.
(55) Yuan, H.; Chen, J.; Wang, H.; Hu, P. Activity Trend for Low-Concentration NO Oxidation at Room Temperature on Rutile-Type Metal Oxides. *ACS Catal.* **2018**, *8*, 10864−10870.

https://doi.org/10.1021/jacsau.4c00377
JACS Au 2024, 4, 3038−3048

(56) Chen, J.; Mao, Y.; Wang, H.; Hu, P. A. A Simple Method To Locate the Optimal Adsorption Energy for the Best Catalysts Directly. *ACS Catal.* **2019**, *9*, 2633−2638.
(57) Chen, J.; Jia, M.; Wang, J.; Hu, P.; Wang, H. Breaking through the Peak Height Limit of the Volcano-Shaped Activity Curve for Metal Catalysts: Role of Distinct Surface Structures on Transition Metal Oxides. *J. Phys. Chem. C* **2022**, *126*, 183−191.
(58) Li, W.; Lou, Z.; Yuan, H.; Yang, H. G.; Wang, H. Oriented Design of Triple Atom Catalysts for Electrocatalytic Nitrogen Reduction with the Genetic-algorithm-based Global Optimization Method Driven by First Principles Calculations. *J. Mater. Chem. A* **2022**, *10*, 16106−16114.
(59) Kresse, G.; Furthmüller, J. Efficient Iterative Schemes for Ab Initio Total-Energy Calculations Using a Plane-Wave Basis Set. *Phys. Rev. B: Condens. Matter Mater. Phys.* **1996**, *54*, 1169−1186.
(60) Perdew, J. P.; Ruzsinszky, A.; Csonka, G. I.; Vydrov, O. A.; Scuseria, G. E.; Constantin, L. A.; Zhou, X.; Burke, K. Restoring the Density-Gradient Expansion for Exchange in Solids and Surfaces. *Phys. Rev. Lett.* **2008**, *100*, 136406.
(61) Kresse, G.; Joubert, D. From Ultrasoft Pseudopotentials to the Projector Augmented-Wave Method. *Phys. Rev. B: Condens. Matter Mater. Phys.* **1999**, *59*, 1758−1775.
(62) Ranea, V. A.; Quiña, P. L. D.; Yalet, N. M. A DFT+U Study, Including the Van Der Waals Interaction, on the Adsorption of XO_2 Molecules on the V_2O_5(001) surface (x = S, N, O, C). *Surf. Sci.* **2019**, *679*, 110−116.
(63) Blum, R. P.; Niehus, H.; Hucho, C.; Fortrie, R.; Ganduglia-Pirovano, M. V.; Sauer, J.; Shaikhutdinov, S.; Freund, H. J. Surface Metal-Insulator Transition on a Vanadium Pentoxide (001) Single Crystal. *Phys. Rev. Lett.* **2007**, *99*, 226103.
(64) Alavi, A.; Hu, P.; Deutsch, T.; Silvestrelli, P. L.; Hutter, J. CO Oxidation on Pt(111): An Ab Initio Density Functional Theory Study. *Phys. Rev. Lett.* **1998**, *80*, 3650−3653.
(65) Michaelides, A.; Liu, Z. P.; Zhang, C. J.; Alavi, A.; King, D. A.; Hu, P. Identification of General Linear Relationships between Activation Energies and Enthalpy Changes for Dissociation Reactions at Surfaces. *J. Am. Chem. Soc.* **2003**, *125*, 3704−3705.
(66) Chen, J.; Jia, M.; Hu, P.; Wang, H. CATKINAS: A Large-scale Catalytic Microkinetic Analysis Software for Mechanism Auto-analysis and Catalyst Screening. *J. Comput. Chem.* **2021**, *42*, 379−391.
(67) Chen, J.; Jia, M.; Lai, Z.; Hu, P.; Wang, H. SSIA: A Sensitivity-supervised Interlock Algorithm for High-performance Microkinetic Solving. *J. Chem. Phys.* **2021**, *154*, 024108.
(68) Chen, J.; Mao, Y.; Wang, H.; Hu, P. Reversibility Iteration Method for Understanding Reaction Networks and for Solving Microkinetics in Heterogeneous Catalysis. *ACS Catal.* **2016**, *6*, 7078−7087.
(69) Xie, W.; Xu, J.; Chen, J.; Wang, H.; Hu, P. Achieving Theory-Experiment Parity for Activity and Selectivity in Heterogeneous Catalysis Using Microkinetic Modeling. *Acc. Chem. Res.* **2022**, *55*, 1237−1248.
(70) Nørskov, J. K.; Rossmeisl, J.; Logadottir, A.; Lindqvist, L.; Kitchin, J. R.; Bligaard, T.; Jónsson, H. Origin of the Overpotential for Oxygen Reduction at a Fuel-Cell Cathode. *J. Phys. Chem. B* **2004**, *108*, 17886−17892.
(71) Garza, A. J.; Bell, A. T.; Head-Gordon, M. Mechanism of CO_2 Reduction at Copper Surfaces: Pathways to C_2 Products. *ACS Catal.* **2018**, *8*, 1490−1499.
(72) Chan, K.; Nørskov, J. K. Electrochemical Barriers Made Simple. *J. Phys. Chem. Lett.* **2015**, *6*, 2663−2668.
(73) Chan, K.; Nørskov, J. K. Potential Dependence of Electrochemical Barriers from ab Initio Calculations. *J. Phys. Chem. Lett.* **2016**, *7*, 1686−1690.
(74) Long, J.; Guo, C.; Fu, X.; Jing, H.; Qin, G.; Li, H.; Xiao, J. Unveiling Potential Dependence in NO Electroreduction to Ammonia. *J. Phys. Chem. Lett.* **2021**, *12*, 6988−6995.

https://doi.org/10.1021/jacsau.4c00377
JACS Au 2024, 4, 3038−3048